Geothermics 124 (2024) 103123

Contents lists available at ScienceDirect

Geothermics

journal homepage: www.elsevier.com/locate/geothermics

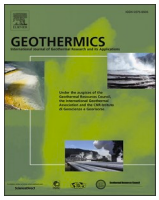

Analytical solution for the simulation of ground thermal conditions around planar trench collectors

Adinda Van de Ven [a,*], Peter Bayer [b], Roland Koenigsdorff [a]

[a] Hochschule Biberach (HBC), Institute for Building and Energy Systems (IGE), Karlstraße 11, 88400 Biberach an der Riß, Germany
[b] Department of Applied Geology, Martin Luther University Halle-Wittenberg, Halle, Germany

ARTICLE INFO

Keywords:
Ground heat collector
Trench collector
Thermal response test
Simulation and modelling
g-function

ABSTRACT

Vertical planar installations in shallow ground are uncommon technological variants for geothermal heat supply. Still, they are of increasing interest when depth and space restrictions do not allow the drilling of boreholes or the installation of horizontal collectors. This work is dedicated to plate-shaped closed-loop heat exchangers that are installed in trenches at a few meters depth. A novel three-dimensional analytical model is presented that accounts for the thermal properties as well as seasonal temperature variation in the ground. The model represents the trench collector as a finite plane source with a specific thermal resistance to simulate the mean temperature of the circulating heat carrier fluid. Both, a detailed dimensional analysis and a successful comparison to numerical simulation are presented. Even though only conductive heat transport is simulated, the model could be validated to the conditions observed at an experimental field site with a trench collector installed at Biberach, Germany. The presented analytical method can serve as an ideal tool for the fast dimensioning of vertical planar heat collectors in practice, and it represents a fundamental framework for the integration of advection or latent heat transfer in frozen ground.

1. Introduction

Ground heat collectors represent a family of closed-loop devices used for feeding ground source heat pumps (GSHP). As a common feature, they are installed at only a few meters depth, where they still experience seasonal temperature fluctuations. There are various types of ground heat collectors such as horizontal ground heat collectors, trench collectors, or geothermal baskets. Hou et al. (2022) classified them according to their geometry into four categories: linear-loops, slinky-coils, helical-coils and others (e.g. plate, tunnel-lining). Each geometry can be installed either vertically or horizontally, and either compactly in trenches or covering a wide area in the subsurface. Obviously, the ideal choice is highly dependent on the available space, and for instance, horizontal collectors are more common in rural areas than in densely populated cities. The state of the art in this field reveals that a growing number of geometries are applied in practice, while appropriate planning tools are lacking. This is due to the challenge of sufficiently resolving the heat transport processes in shallow ground to predict the performance of a given geometry. Therefore, further development of models that can reliably simulate the full system, and which are validated by experimental field measurements, is recommended to increase accuracy, reliability, safety and efficiency of the GSHPs (Hou et al. 2022; Rashid et al. 2023). This motivates the present study.

This paper focuses on three-dimensional analytical modelling of plate-shaped heat exchangers installed vertically in trenches. Recent field applications of these technological variants are reported for instance by Suft and Bertermann (2022) and Oh and Beckers (2023). Analytical models in particular are appealing due to their computational efficiency and compactness in comparison to numerical implementations. This has been demonstrated for example for the simulation of related geothermal devices such as slinky coils implemented as shallow horizontal heat exchangers in vertical arrangement by Xiong et al. (2015) and in horizontal orientation by Larwa et al. (2019). Another related variant of growing interest is the vertical energy wall, with numerical simulation concepts presented by Kürten et al. (2015) and Gerola et al. (2023). For the selected vertical trench geometry in our work, so far only a two-dimensional, analytical model is available (Ciriello et al. 2015b). Aside from this, Bortoloni and Bottarelli (2015) used an analytical solution based on the line source method, which is assumed to be an equivalent slinky-coil having the same heat transfer surface per trench length. Compared with their two-dimensional numerical model, they achieve promising results for the design minimum temperature. Further related work deals with numerical simulations or

* Corresponding author.
E-mail address: vandeven@hochschule-bc.de (A. Van de Ven).

https://doi.org/10.1016/j.geothermics.2024.103123
Received 18 April 2024; Received in revised form 1 July 2024; Accepted 22 July 2024
Available online 20 August 2024

Glossary

d_c	thickness of the trench collector, m
d_h	hydraulic diameter, m
Fo	Fourier number (dimensionless time)
h	heat transfer coefficient, W/(m^2·K)
H_c	height of the collector, m
H_{inst}	installation depth and upper level of the collector, m
H_{tot}	total depth or bottom of the collector. It is the sum of the installation depth and the collector height, m
L_c	length of the collector, m
Nu	Nusselt number
Pr	Prandtl number
$\dot{Q}$	heat injection (positive) or extraction (negative) rate, W
$\dot{q}$	specific heat injection (positive) or extraction (negative) rate, w/m^2
Re	Reynolds number
R	thermal resistance, (m^2·K)/W
R_b	borehole resistance, (m·K)/W
R_h	convective resistance between the fluid and collector material, (m^2·K)/W
^1R_c	resistance between the mean fluid temperature and the temperature at the collector wall of a single collector element, (m^2·K)/W
t	time, s
t_p	period, s
t_0	phase constant: time of the year at which the temperature of the earth's surface reaches its minimum, s
T	temperature, °C
ΔT_{sp}	Temperature spread between the collector inlet and outlet temperatur, K
ΔT	temperature difference, K
ΔT_{am}	annual amplitude of the mean earth surface temperature, K
x, y, z	space coordinates, where the temperature is evaluated, m

Greek symbols

α	thermal diffusivity, m^2/s
λ	thermal conductivity, W/(m·K)
θ	dimensionless temperature response

Subscripts

a	referring to the air properties
analyt	referring to the analytical model
c	referring to the collector
cw	referring to the collector wall
fl	referring to the physical properties of the fluid
FPS	referring to the Finite Plane Source (Solution)
g	referring to the ground or subsurface
i	referring to the inlet of the collector
ia	referring to the interaction
measurement	referring to the measurement data
num.	referring to the numerical simulation(s)
o	referring to the outlet of the collector
pp	referring to the polypropylene material of the collector
s	reffering to the properties of the solid matrix
w	reffering to the properties of the water

Superscripts

–	referring to the mean value
*	referring to the dimensionless coordinates
‘	referring to the location of the source

experimental measurements for feasibility studies, the comparison of flat-panel heat exchangers with other geometries and performance analysis (Amadeh et al. 2020; Bottarelli 2013; Bottarelli et al. 2014; Bottarelli et al. 2019; Bottarelli and Di Federico 2012; ; Cao et al. 2018, 2018; Ciriello et al. 2015b; Ciriello et al. 2015a; Gabrielli and Bottarelli 2016, 2016; Habibi et al. 2020; Schwarz et al. 2022; Zhou et al. 2021). For example, Habibi et al. (2020) revealed by numerical simulation the benefits of flat-panel vertical collectors in comparison to linear heat exchangers. However, to the best of our knowledge, no analytical three-dimensional model that accurately describes a plate-shaped trench collector has been developed by this time. Thus, our objective is to close this gap. A new analytical model of planar ground heat collectors installed vertically in trenches for heat conduction in the subsurface is presented and validated with numerical simulations and experimental data.

2. Materials and methods

2.1. Analytical model

2.1.1. Finite plane source

Heat conduction in the subsurface influenced by a planar trench collector is mathematically best represented by a finite plane source (FPS) with an isothermal boundary condition (Fig. 1). Analogous to the popular finite line source used for the thermal design of borehole heat exchangers (Cimmino 2018; Fascì et al. 2021; Rivera et al. 2015), the FPS is deduced from the three-dimensional, transient heat conduction equation:

$$\frac{\partial T}{\partial t} = \alpha \left(\frac{\partial^2 T}{\partial x^2} + \frac{\partial^2 T}{\partial y^2} + \frac{\partial^2 T}{\partial z^2} \right) \tag{1}$$

in which t is time in s, $T(x,y,z,t)$ is temperature in K (or °C) and α is the thermal diffusivity in m^2/s. A planar heat source of strength $\dot{q}$ in $\frac{W}{m^2}$ is applied at $y = 0$ (see Fig. 1). It has a constant value S within the dimensions of the vertical planar trench collector, i.e. from 0 to L_c in m in x-direction and from H_{inst} to $(H_{inst} + H_c)$ in m in z-direction (see Fig. 1), and is zero outside:

$$\dot{q}(x,y,z,t) = \begin{cases} S \text{ for } 0 \le x \le L_c \wedge y = 0 \wedge H_{\text{inst}} \le z \le (H_{\text{inst}} + H_c) \\ 0 \end{cases} \tag{2}$$

Furthermore, the boundary conditions at infinity, at the ground surface, and the initial condition are given in Eqs. (3) and (4), respectively:

$$T|_{|x|\to\infty} = T|_{|y|\to\infty} = T|_{z\to\infty} = T|_{z=0} = 0 \tag{3}$$

$$T|_{t=0} = 0 \tag{4}$$

Taking the instantaneous point source as a fundamental solution of potential theory (Carslaw and Jaeger 1980), it can be used to solve the above-described problem for heat conduction. For this, the instantaneous point source has to be integrated over time from 0 to t to obtain the continuous point source at x', y', z' in an infinite solid (Carslaw and Jaeger 1980). Its solution is given as:

$$T(x,y,z,t) = \frac{\dot{Q}}{4\,\pi\,\lambda} \frac{erfc\left(\frac{\sqrt{(x-x')^2+(y-y')^2+(z-z')^2}}{2\sqrt{\alpha\, t}} \right)}{\sqrt{(x-x')^2+(y-y')^2+(z-z')^2}} \tag{5}$$

where the temperature $T(x,y,z,t)$ is considered to be the solution for a point source if heat is liberated at the rate $\dot{Q}$ (in W) per unit time from $t = 0$ to $t = t$ at the location (x', y', z'). Here x, y, z are the evaluation points,

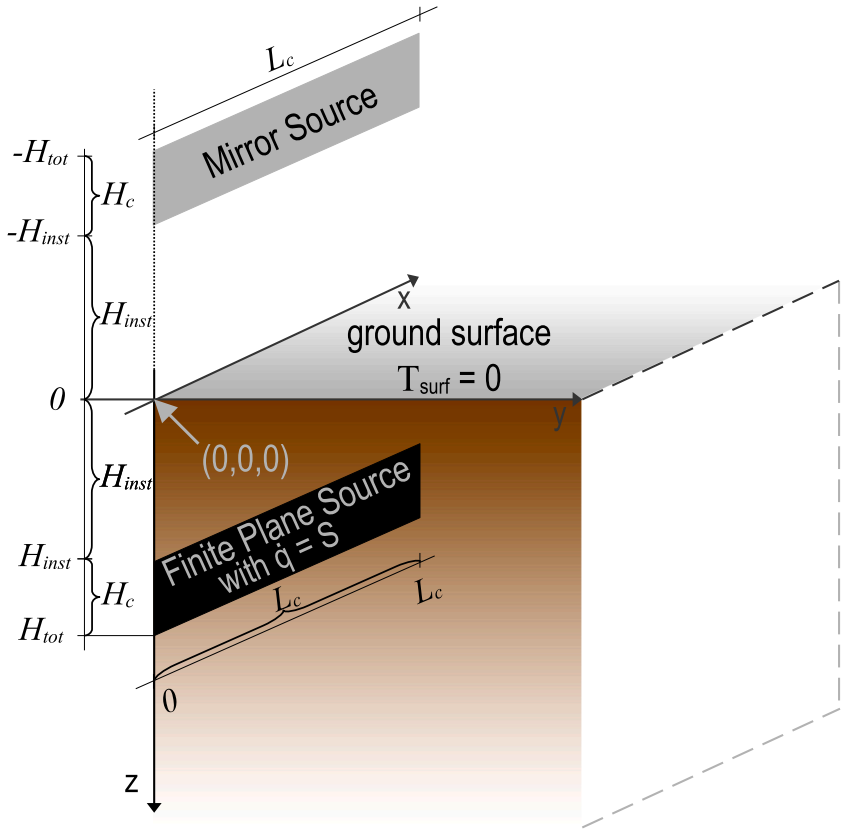

Fig. 1. Geometrical settings for the finite plane source in a semi-infinite solid with an isothermal boundary to simulate a vertical trench collector.

whereas x', y', z' define the location of the heat source. Furthermore, λ is the thermal conductivity in $\frac{W}{mK}$.

Next, the continuous point source solution must be integrated to the required dimensions of the collector under consideration, to gain the solution of the FPS in an infinite solid. With a collector of length L_c and height H_c, i.e. the plane source is located at $(0 \le x' \le L_c)$, $(y' = 0)$, $(0 \le z' \le H_c)$ (see Fig. 1), the integral formulation reads as:

$$T(x,y,z,t) = \frac{\dot{q}}{4\,\pi\,\lambda} \int_0^{L_c} \int_0^{H_c} \frac{erfc\left(\frac{\sqrt{(x-x')^2+(y-y')^2+(z-z')^2}}{2\sqrt{\alpha\, t}}\right)}{\sqrt{(x-x')^2+(y-y')^2+(z-z')^2}}\, dz'\, dx' \qquad (6)$$

Finally, the method of image is used to create the solution within a semi-infinite solid with an isothermal boundary condition at $z = 0$, which represents the ground surface as depicted in Fig. 1. The solution of the FPS with an isothermal boundary condition at the subsurface, T_{FPS}, reads:

$$T_{FPS}(x,y,z,t) = \frac{\dot{q}}{4\pi\lambda} \int_0^{L_c} \int_{H_{inst}}^{H_{inst}+H_c} \frac{erfc\left(\frac{\sqrt{(x-x')^2+(y-y')^2+(z-z')^2}}{2\sqrt{\alpha t}}\right)}{\sqrt{(x-x')^2+(y-y')^2+(z-z')^2}} - \frac{erfc\left(\frac{\sqrt{(x-x')^2+(y-y')^2+(z+z')^2}}{2\sqrt{\alpha t}}\right)}{\sqrt{(x-x')^2+(y-y')^2+(z+z')^2}}\, dz'\, dx' \qquad (7)$$

where H_{inst} is the installation depth of the trench collector in m, i.e. the distance between the ground surface and the upper edge of the ground heat collector. Eq. (7) is the solution of Eq. (1) for the homogeneous boundary condition at $z = 0$ and allows the determination of the temperature at any point (x, y, z) around the planar collector apart from the location of the source for times $t > 0$. For design purposes, however, the mean temperature at the wall of the trench collector $\overline{T}_{cw}\left(\frac{d_c}{2}, t\right)$ is to be considered and can be calculated by Eq. (8) for $y = \frac{d_c}{2}$. d_c is the thickness of the ground heat collector in m, which in our specific case is 0.006 m (see Fig. 4). Since the source itself has no width, it is centred so that an evaluation at the collector wall corresponds to $y = \frac{d_c}{2}$ *or* $y = \frac{-d_c}{2}$. In this case, it is sufficient to consider only one side of the collector wall, as the heat transfer is symmetrical.

$$\overline{T}_{FPS}(y,t) = \frac{\dot{q}}{4\pi\lambda L_c H_c} \int_0^{L_c}\int_{H_{inst}}^{H_{inst}+H_c}\int_0^{L_c}\int_{H_{inst}}^{H_{inst}+H_c} \frac{erfc\left(\frac{\sqrt{(x-x')^2+(y-y')^2+(z-z')^2}}{2\sqrt{\alpha t}}\right)}{\sqrt{(x-x')^2+(y-y')^2+(z-z')^2}} - \frac{erfc\left(\frac{\sqrt{(x-x')^2+(y-y')^2+(z+z')^2}}{2\sqrt{\alpha t}}\right)}{\sqrt{(x-x')^2+(y-y')^2+(z+z')^2}} dz'dx'dzdx. \tag{8}$$

By simplifying the quadruple integral in Eq. (8) to a sum of only double and single integrals, the formula becomes more manageable. The reduction of the multiple integrals in Eq. (8) leads to the long but computationally optimised Eq. (A I) contained in the appendix. Evaluating Eq. (8) at $y = \frac{d_c}{2}$ results in the mean collector wall temperature $\overline{T}_{cw}$.

2.1.2. Dimensional analysis

The dimensional analysis of the given heat conduction problem facilitates, analogous to the common g-functions of borehole heat exchangers (Cimmino 2018; Eskilson 1987; Miocic et al. 2024; Rivera et al. 2017), the development of dimensionless response functions at the collector wall. The use of these functions enables a broad range of application of a certain solution independent of case-specific geometrical and thermal properties. The total height from the ground surface to the bottom of the ground heat collector H_{tot} in m (see Fig. 1) is used for nondimensionalisation of all geometry parameters and is calculated as follows:

$$H_{tot} = H_{inst} + H_c \tag{9}$$

This height is chosen for the non-dimensionalisation since it comprises two relevant geometrical parameters influencing the dimensionless temperature response, i.e. the installation depth H_{inst} and the collector height H_c. These heights are governing parameters for the heat transfer between the collector and the ground surface, whereas the influence of the collector length L_c is less pronounced, because typically L_c is larger than the heights. Particularly with very long collectors or several collectors in a row, the influence of L_c becomes increasingly less relevant, approaching a two-dimensional situation which would result in values of the non-dimensional coordinates towards zero if L_c was used for non-dimensionalisation.

Then, the following dimensionless variables are used in the dimensional analysis:

$$x^* = \frac{x}{H_{tot}} \qquad y^* = \frac{y}{H_{tot}} = \frac{d_c}{2H_{tot}} \qquad z^* = \frac{z}{H_{tot}} \tag{10}$$

$$x'^* = \frac{x'}{H_{tot}} \qquad y'^* = \frac{y'}{H_{tot}} = 0 \qquad z'^* = \frac{z'}{H_{tot}} \tag{11}$$

$$Fo_{H_{tot}} = \frac{\alpha\, t}{H_{tot}^{\,2}} \tag{12}$$

$$\theta(Fo_{H_{tot}}) = \Delta T(t)\ \frac{\lambda}{\dot{q}\, H_{tot}} \tag{13}$$

where the dimensionless coordinates $x^*, y^*, z^*, x'^*, y'^*, z'^*$ are marked by a superscript asterisk, $Fo_{H_{tot}}$ corresponds to the dimensionless time and $\theta(Fo_{H_{tot}})$ is the dimensionless temperature response of the ground heat collector.

Hence, the dimensionless form of Eq. (1) is defined as

$$\frac{\dot{q}H_{tot}}{\lambda}\frac{\alpha}{H_{tot}^{\,2}}\frac{\partial\theta}{\partial Fo_{H_{tot}}} = \frac{\dot{q}H_{tot}}{\lambda}\frac{1}{H_{tot}^{\,2}}\alpha\left(\frac{\partial^2\theta}{\partial x^{*2}}+\frac{\partial^2\theta}{\partial y^{*2}}+\frac{\partial^2\theta}{\partial z^{*2}}\right)$$
$$\frac{\partial\theta}{\partial Fo_{H_{tot}}} = \left(\frac{\partial^2\theta}{\partial x^{*2}}+\frac{\partial^2\theta}{\partial y^{*2}}+\frac{\partial^2\theta}{\partial z^{*2}}\right) \tag{14}$$

It can be deduced that the dimensionless temperature response resulting from the FPS for one trench collector depends on the Fourier number, the dimensionless time, Eq. (12) and the following dimensionless geometrical parameters:

$$\frac{L_c}{H_{tot}} \tag{15}$$

$$\frac{H_{inst}}{H_{tot}} \tag{16}$$

$$\frac{d_c}{2\,H_{tot}} \tag{17}$$

Using Eq. (8) and the dimensional analysis, the dimensionless temperature response at the collector wall of the continuous FPS solution with an isothermal boundary condition at the ground surface is derived:

$$\overline{\theta}\left(\frac{d_c}{2H_{tot}}, x^*, z^*, x'^*, z'^*, Fo_{H_{tot}}\right) = \frac{H_{tot}}{4\pi\frac{L_c}{H_{tot}}\left(1-\frac{H_{inst}}{H_{tot}}\right)} \int_0^{\frac{L_c}{H_{tot}}}\int_{\frac{H_{inst}}{H_{tot}}}^{1}\int_0^{\frac{L_c}{H_{tot}}}\int_{\frac{H_{inst}}{H_{tot}}}^{1} \frac{erfc\left(\frac{\sqrt{(x^*-x'^*)^2+\left(\frac{d_c}{2H_{tot}}\right)^2+(z^*-z'^*)^2}}{2\sqrt{Fo_{H_{tot}}}}\right)}{\sqrt{(x^*-x'^*)^2+\left(\frac{d_c}{2H_{tot}}\right)^2+(z^*-z'^*)^2}} - \frac{erfc\left(\frac{\sqrt{(x^*-x'^*)^2+\left(\frac{d_c}{2H_{tot}}\right)^2+(z^*+z'^*)^2}}{2\sqrt{Fo_{H_{tot}}}}\right)}{\sqrt{(x^*-x'^*)^2+\left(\frac{d_c}{2H_{tot}}\right)^2+(z^*+z'^*)^2}} dz'^*dx'^*dz^*dx^* \tag{18}$$

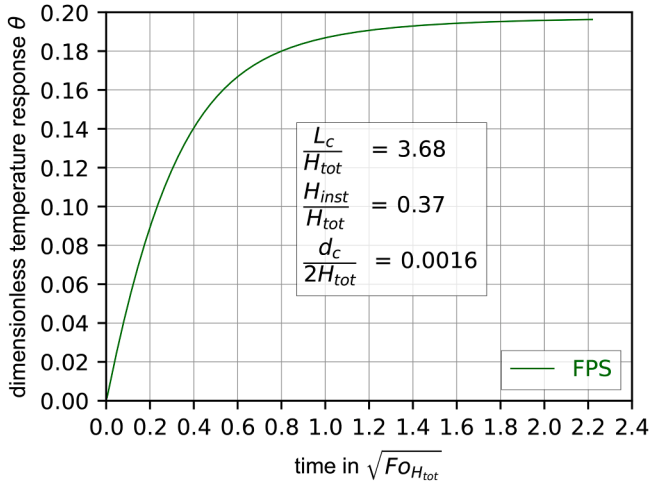

Fig. 2. Dimensionless temperature response of the FPS with a heat injection rate at the source and a source geometry corresponding to the one of the experimental plant at the Biberach University of Applied Sciences (see technical details given in Section 2.3).

An exemplary curve of the dimensionless temperature response for an experimental plant (described in detail in Section 2.3) is shown in Fig. 2.

2.1.3. Seasonal temperature variation

Generally, ground heat collectors are installed at a depth of 1 to 1.5 m below the ground surface and can affect the subsurface at a depth of 3 to 5 m (Koenigsdorff 2011). Therefore, the annual temperature oscillation at the ground surface and its impact at the installation depth have to be considered. Since the temperature in these depths varies within a broad range, Kusuda and Achenbach (1965) proposed Eq. (19) to calculate the seasonal varying ground temperature $T_g(z,t)$ depending on its depth z in m:

$$T_g(z,t) = \overline{T}_a - \Delta T_{am}\, e^{-z\sqrt{\frac{\pi}{t_p\,\alpha}}} \cos\left(\frac{2\,\pi}{t_p}\left[t - t_0 - \frac{z}{2}\sqrt{\frac{t_p}{\pi\,\alpha}}\right]\right) \tag{19}$$

The phase constant t_0 in Eq. (19) corresponds to the time of the year in s at which the temperature of the ground surface reaches its minimum. The considered time period t_p in s is one year, as after this period the seasonal oscillation restarts. This oscillation with the amplitude ΔT_{am} is subtracted from the annual mean air temperature $\overline{T}_a$. As can be seen in Fig. 3, the seasonal temperature at a specific time of the year can vary by several degrees over the collector height. For example, at the end of the second month the undisturbed subsurface temperature varies between 3.6 °C at the installation depth and 6.4 °C at the bottom of the collector, whereas at the end of the fourth month there is barely a temperature difference. Analysing Eq. (19), the damping of the ground surface temperature oscillation depends on $-z\sqrt{\frac{\pi}{t_p\,\alpha}}$, which corresponds to $-\sqrt{\frac{\pi}{Fo_z}}$, i.e. the damping includes the dimensionless time Fo_z. Only for values of Fo_z smaller than 0.025 the seasonal oscillation is regarded to be negligible, larger values show a clear influence of the seasonal temperature oscillation. Since the undisturbed subsurface temperature is crucial for both the determination of the minimum temperature and for natural regeneration and varies within a broad range over the collector height, it is important to average this temperature spatially (over the collector height). The spatial averaging of the seasonal temperature variation of the undisturbed subsurface within the installation depth is carried out over the collector height, starting at the installation depth H_{inst} and reaching down to the collector bottom edge H_{tot}. Eqs. (20) and (21) specify the average of the seasonal undisturbed temperature over the collector height:

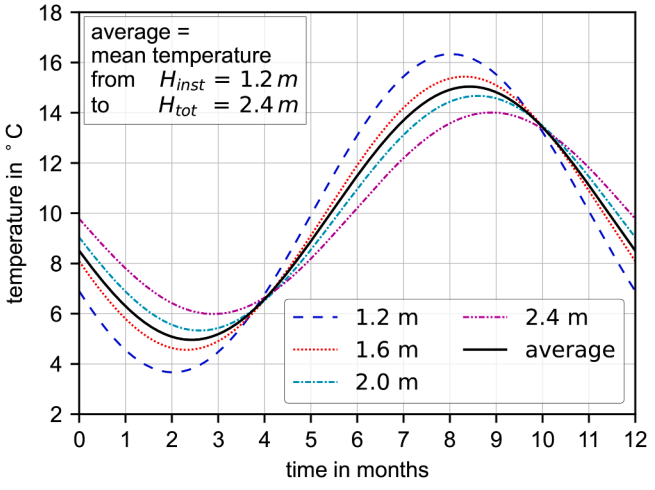

Fig. 3. Seasonal temperature variations of the subsurface at various depths over the collector height and its mean value for the parameters defined in Table 1.

$$\overline{T}_g(t) = \overline{T}_a + \Delta\overline{T}_g(t) \tag{20}$$

$$\Delta\overline{T}_g(t) = \frac{-\Delta T_{am}}{2\,H_c\sqrt{\frac{\pi}{t_p\,\alpha}}} \left\{ \begin{array}{l} e^{-H_{inst}\sqrt{\frac{\pi}{t_p\,\alpha}}} \left[\begin{array}{l} \sin\left(\frac{2\,\pi}{t_p}(t-t_0) - H_{inst}\sqrt{\frac{\pi}{t_p\,\alpha}}\right) \\ +\cos\left(\frac{2\,\pi}{t_p}(t-t_0) - H_{inst}\sqrt{\frac{\pi}{t_p\,\alpha}}\right) \end{array} \right] \\ -e^{-H_{tot}\sqrt{\frac{\pi}{t_p\,\alpha}}} \left[\begin{array}{l} \sin\left(\frac{2\,\pi}{t_p}(t-t_0) - H_{tot}\sqrt{\frac{\pi}{t_p\,\alpha}}\right) \\ +\cos\left(\frac{2\,\pi}{t_p}(t-t_0) - H_{tot}\sqrt{\frac{\pi}{t_p\,\alpha}}\right) \end{array} \right] \end{array} \right\} \tag{21}$$

with $\overline{T}_g(t)$ being the spatial mean undisturbed subsurface temperature in °C over the installation depth of the trench collector and $\Delta\overline{T}_g(t)$ is the spatial average (over the installation depth) of the temperature change of the seasonal oscillation. Eq. (19) is a quasi-stationary solution of Eq. (1) for the inhomogeneous temperature boundary condition which corresponds to Eq. (19) for $z = 0$.

For a trench collector buried at a depth of 1.2 m, a collector height of 1.2 m and the properties listed in Table 1, the seasonal temperature variations in the collector depth and its mean temperature variation are depicted in Fig. 3.

2.1.4. Ground heat exchanger resistance

Analogous to referring to the thermal resistance R_b of borehole heat exchangers (Eskilson 1987; Hellström 1991; Lamarche 2021; Ozudogru et al. 2014; Wagner et al. 2013; Yoon et al. 2014) the heat transfer through the ground heat collector itself is modelled with a so-called collector resistance, R_c (Van de Ven et al. 2018). All thermal resistances in this paper have the unit $\frac{m^2K}{W}$. A cross-section of the collector geometry, a twin-wall sheet, is depicted in Fig. 4. Fig. 4b) shows the analytical resistance model for one collector element (one fluid channel with corresponding plate section), which consists of a convective resistance R_h between fluid and collector material and a conductive resistance R_{pp} through the polypropylene. These resistances are connected in series. The convective resistance R_h can be defined analytically, whereas the conductive resistance R_{pp} is defined by numerical simulations and both are combined by an analytical resistance model. The entire model is based on assumptions which are described hereinafter. The first assumption is a uniform flow through each element of the trench collector, which means that the heat carrier fluid temperature in each channel is uniform as well. Thus, the interaction between the channels is considered negligible, i.e., R_{ia} may be omitted. As a consequence, adiabatic boundary conditions between the collector elements as depicted in Fig. 4a) allow a parallel connection of all element resistances ${}^1R_c$ except for the five elements each at the top and at the bottom of the trench collector. These are excluded since no flow occurs through these channels for safety reasons and are thus treated as inactive. Accordingly, in the model, the 6th element both from the top and the bottom has only one adiabatic boundary towards the neighbouring active element. This means that two kinds of conductive resistances R_{pp} must be considered

Table 1
Parameters used to calculate undisturbed subsurface temperatures.

Parameter description	Value	Unit
Annual mean air temperature $\overline{T}_a$	10	°C
Annual amplitude of the mean ground surface temperature ΔT_{am}	10	K
Phase constant t_0	840	h
Period t_p	8760	h
Thermal diffusivity of the subsurface α	0.002477064	m^2/h

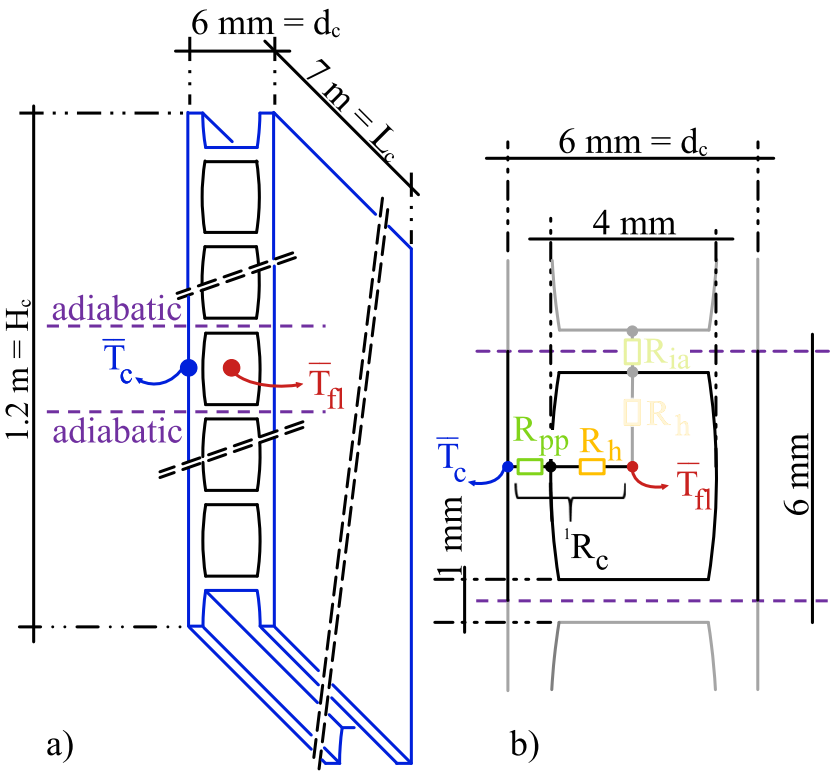

Fig. 4. a) Geometry and cross-section of the trench collector in a three-dimensional perspective, and b) the analytical resistance model for one channel with two adiabatic boundaries.

and as a consequence two numerical simulations must be carried out for the different collector elements: one for the centre element with two adiabatic boundary conditions, and one for a corner element which has one adiabatic boundary condition and borders on five non-flow-through elements on the other side. Furthermore, the boundary condition towards the subsurface is set to have a constant temperature, whereas the collector interior boundary of the active elements is simulated with a Cauchy boundary condition. The collector consists of 199 elements, 189 of which are active and 187 of which correspond to the resistance model in Fig. 4b).

The heat transfer coefficient h in $\frac{W}{m^2K}$ is the inverse of the convective resistance R_h and is calculated by Eqs. (22) and (23) for laminar flow in the collector. Due to the small chambers of the collector, only a laminar flow will occur within this kind of trench collector. Thus, h can be calculated from (Schramek et al. 2005).

$$h = \frac{Nu\ \lambda}{d_h} \tag{22}$$

with

$$Nu = \left[49.028 + 4.173\ Re\ Pr\ \frac{d_h}{L_c}\right]^{0.333} \quad for\ Re < 2320 \tag{23}$$

where Nu is the dimensionless Nusselt number, characterising the convective heat transfer, d_h the representative dimension in m, which in this specific case is the hydraulic diameter of the collector channel, and λ is the thermal conductivity of the fluid in $\frac{W}{mK}$. In order to calculate the Nusselt number Nu, the Prandtl number Pr is needed. Furthermore, it hast to be checked if the condition for the Reynolds number Re is fulfilled. Considering material properties of a mixture of water and ethylene glycol with 25% glycol for the fluid, a nominal volume flow of 6 l/min though the trench collector and a Reynolds number of 35, the heat transfer coefficient h reaches a value of 368.46 W/(m^2 K) at a fluid temperature of 0 °C. In order to determine the collector resistance, the results of the numerical simulations from Van de Ven et al. (2018) are used, resulting in a temperature-specific heat flux density of 246.58 W/(m^2 K) and 41.17 W/(m^2 K), for each middle element and each edge element, respectively. With these results and the installation area serving as a reference surface, the overall collector resistance R_c is 0.00429 (m^2 K)/W. Using the collector resistance R_c and the heat extraction or injection rate $\dot{q}$, the temperature change due the trench collector resistance, ΔT_{R_c}, is calculated as:

$$\Delta T_{R_c} = \dot{q} R_c \tag{24}$$

2.1.5. *Analytical algorithm for ground thermal conditions around a planar trench collector*

The major benefit of the analytical model presented here is the fast calculation of the collector outlet temperature. The collector outlet temperature is often the main limitation in the design of such systems due to operational safety or to avoid environmental damage (Ramming 2007; Verein Deutscher Ingenieure e.V., 2019). The prerequisite for its calculation is that the heat extraction rate, the temperature spread over the collector $\Delta T_{sp}(t)$ (difference between fluid inlet and outlet temperature), the thermal subsurface properties, and the collector geometry are given. The heat transfer in the subsurface due to the planar trench collector including the undisturbed seasonal temperature oscillation is decomposed into a homogeneous and an inhomogeneous boundary value problem. In this case, the $T_{FPS}(x,y,z,t)$ is the solution (Eq. (7)) of the homogeneous boundary value problem, while the seasonal temperature oscillation represents the solution (Eq. (19)) of the inhomogeneous boundary value problem (Carslaw and Jaeger 1980). Therefore, the dimensionless temperature response function $\theta\left(\frac{L_c}{H_{tot}}, \frac{H_{inst}}{H_{tot}}, \frac{d_c}{2\ H_{tot}}, Fo_{H_{tot}}\right)$ with the corresponding dimensionless parameters can be selected. Now the temperatures from Sections 2.1.1 and 2.1.3 can be calculated and superposed to determine the mean collector wall temperature $\overline{T}_{cw}(t)$. Thereupon, the temperature change due to the collector resistance as

described in Section 2.1.4 can be applied, so that finally the collector outlet temperature $T_{fl,o}$ is determined as in the following equations:

$$\overline{T}_{fl}(t) = \overline{T}_{g}(t) + \overline{T}_{cw}(t) + \Delta T_{R_c}(t) \tag{25}$$

$$T_{fl,o} = \overline{T}_{fl}(t) - \frac{\Delta T_{sp}(t)}{2} \tag{26}$$

The collector outlet temperature $T_{fl,o}$ has to be determined in the design phase, since this temperature is limited, e.g. in the VDI-guideline in Germany (Verein Deutscher Ingenieure e.V. 2019).

2.2. Numerical model

The numerical model serves as a reference for the validation of the analytical model. The basic model is set up in COMSOL Multiphysics® using the Heat Transfer in Porous Media module. Since the FPS model simulates heat conduction only in the subsurface, the numerical model does not consider the detailed geometry of the planar trench collector but focuses on the relevant heat transfer processes in the surrounding ground. Therefore, the collector is represented as a planar heat sink/source installed at a depth of 1.2 m below the surface. The seasonal temperature fluctuations at the ground surface are represented using Eq. (19) for the time-dependent temperature variation at the surface by setting $z = 0$ m. The initial temperature distribution of the simulation domain due to the seasonal fluctuations is also calculated by Eq. (19) using $t = 0$ s as a starting point in time. The domain was defined empirically by varying its size, while both the temperature at the collector wall and the dimensionless temperature were monitored for different boundary conditions. Furthermore, the calculation speed is optimised by quartering the simulation domain and using symmetry boundary conditions. As a result of the domain reduction due to symmetry, the heat injection rate specified in COMSOL is halved compared to the analytical model to ensure consistency of both models. In addition to the domain reduction, infinite regions at the border of the domain allow a reduction of the simulation domain whilst avoiding their boundary influence at the collector surface. The grid of the numerical model consists mainly of a free tetrahedral mesh extended by a structured mesh in the infinite regions. At the collector surface, the grid is extremely fine and becomes coarser towards the edge.

2.3. Experimental plant

To validate practical suitability, the proposed analytical model is compared with measurement data of an experimental plant. The experimental plant is located at the Biberach University of Applied Sciences in Biberach (Riß) in southern Germany. The collector is 7 m long, 1.2 m high, 6 mm thick and installed in a trench at a depth of 70 cm below the ground surface. The collector consists of 199 polypropylene channels as depicted in Fig. 4. A more detailed description of the ground heat collector plant and the installed measuring equipment can be found in (Van de Ven et al. unpublished results). In addition to the trench collector and measurement equipment system described in (Van de Ven et al. unpublished results), the TRT device of the Biberach University of Applied Sciences shown in Fig. 5b) is used to increase the inlet temperature in the trench collector while assuring a constant heat transfer rate. Further details on the trench collector itself can be found in planning and operating instructions (MEFA Befestigungs- und Montagesysteme GmbH 2022).

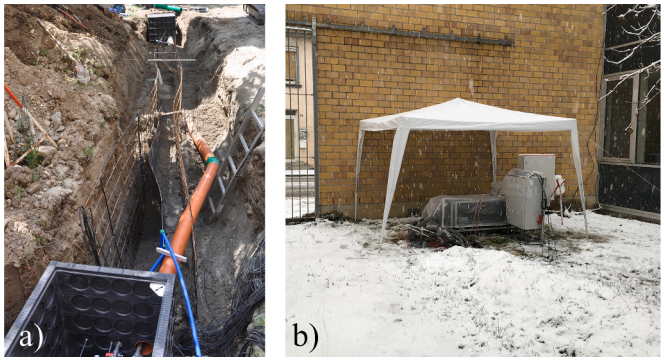

Fig. 5. a) Trench collector and measurement equipment during installation, b) thermal response test device attached to the trench collector plant at the experimental site.

For the validation of the FPS model with measurement data from the experimental plant, the dimensionless temperature response of the FPS model with the dimensionless parameter values matching the ones of the experimental plant is used. The site-specific values are as follows:

$$\frac{L_c}{H_{tot}} = 3.68;\ \frac{H_{inst}}{H_{tot}} = 0.37;\ \frac{d_c}{2\,H_{tot}} = 0.0016 \tag{27}$$

Fig. 2 shows the corresponding dimensionless temperature response for the installed trench collector.

3. Results and discussion

3.1. Verification of the analytical model

For the mathematical verification of the analytical model equations derived here, a period of one year is analysed, as ground heat collectors should be regenerated within one year to ensure the same output in the following year. Note that the collector and subsurface properties for the theoretical investigations in this chapter correspond to recommended installation conditions. Thus, parameter settings for verification as listed in Table 2 are hypothetical and vary from the ones of the experimental plant that is subject to the following chapter.

The verification is carried out systematically. First, a constant heat extraction rate and a constant temperature at the ground surface as in Eq. (8) is investigated followed by the model for the mean seasonal temperature variation in the installation depth as in Eqs. (20) and (21). After that, the combination of both models, i.e. the superposing of the temperature change in Eqs. (8), (20) and (21), is investigated and compared with the corresponding numerical model. Finally, a simulation is carried out considering a six-month collector operation followed by six months of regeneration while including the seasonal temperature variation.

If only the FPS model is compared with the numerical simulation, it

Table 2
Collector and subsurface properties for the comparison of the analytical and numerical model.

Collector properties:			
Collector length	L_c	7	m
Collector height	H_c	1.2	m
Collector thickness	d_c	0.006	m
Installation depth	H_{inst}	1.2	m
Heat load	$\dot{Q}$	-200	W
Subsurface properties:			
Thermal conductivity of the solid matrix	λ_s	1.5	W/(m K)
Porosity	ϕ	0.2	
Density of the solid matrix	ρ_s	2180	kg/m^3
Specific heat capacity of the solid matrix	$c_{p,s}$	1000	J/(kg K)
Thermal conductivity of the groundwater	λ_w	0.58	W/(m K)
Density of the groundwater	ρ_w	1000	kg/m^3
Specific heat capacity of the groundwater	$c_{p,w}$	4200	J/(kg K)
Annual mean surface temperature	$\overline{T}_{g,0}$	10	°C
seasonal temperature oscillation:			
Period	t_p	8760	h
Phase constant	t_0	840	h
Annual amplitude of the surface temperature	ΔT_{am}	10	K

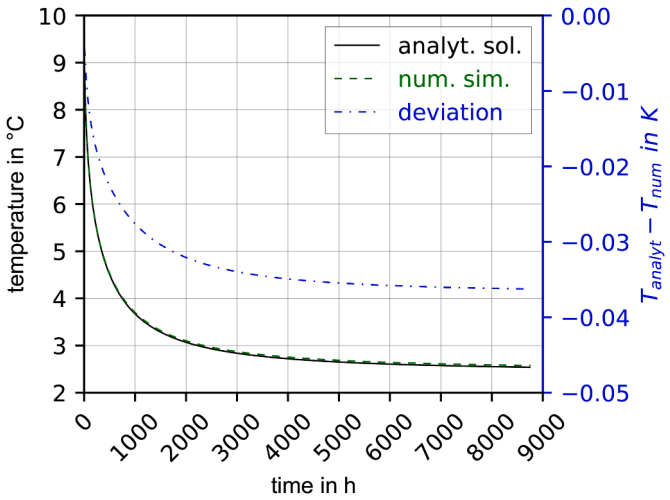

Fig. 6. Comparison of the temperature of the analytical and the numerical model for a constant heat extraction rate and a constant temperature at the ground surface.

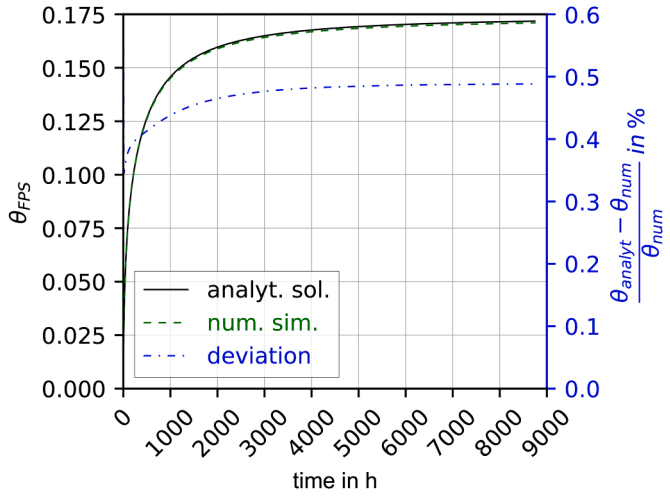

Fig. 7. Comparison of the dimensionless temperature response of the analytical and the numerical model for a constant heat extraction rate and a constant temperature at the ground surface.

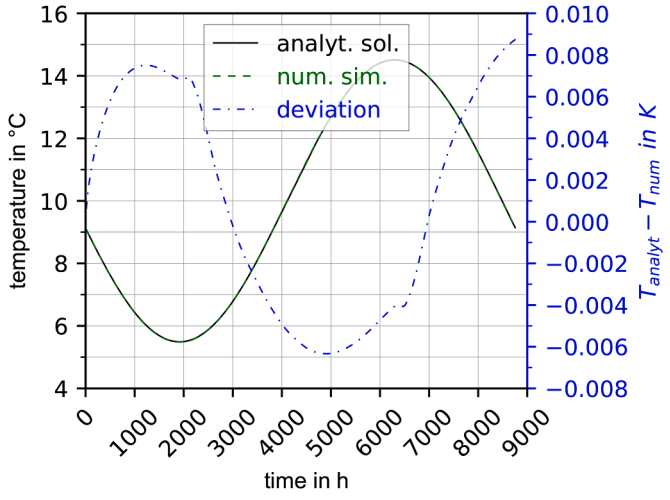

Fig. 8. Comparison of the spatial mean seasonal temperature in the installation depth of the analytical and the numerical model.

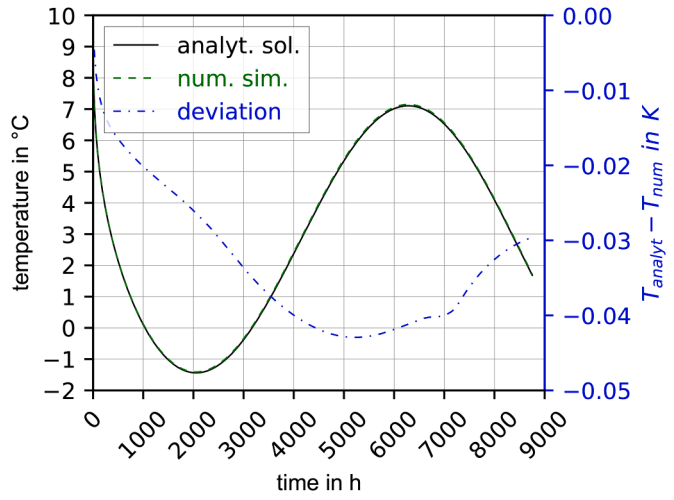

Fig. 9. Comparison of the temperature of the analytical and the numerical model for a constant heat extraction rate and a seasonal temperature variation at the ground surface.

can be seen in Figs. 6 and 7 that both models agree very well. The absolute temperature deviation is less than 0.04 K, and the percentage deviation is less than 0.5% and can therefore be neglected.

The spatial integral mean of the undisturbed subsurface temperature in the installation depth of the trench collector for both the numerical simulation and the analytical solution from Eqs. (20) and (21) are shown in Fig. 8. The deviation between both models reaches a maximum of ca. 0.009 K, which is very small and considered negligible.

For the combination of the model with constant heat extraction and the seasonal temperature variation in the subsurface, the deviation is higher than in the two individual models, as revealed in Fig. 9. However, the maximum deviation is smaller than 0.05 K. This value is so small that it can be considered negligible for practical purposes. This very good agreement proves that by decomposition of the problem in an inhomogeneous and a homogeneous boundary value problem the single solutions can be superposed. If calculation time is considered, the numerical model takes 7 h 48 min. with an Intel Xeon Gold 6230R @ 2.10 GHz processor. In contrast, the analytical model takes less than eight minutes on a standard laptop. The reduction in computing time by a factor of more than 60 clearly shows the advantage of the analytical model.

Typically, a ground heat collector will extract heat during the winter

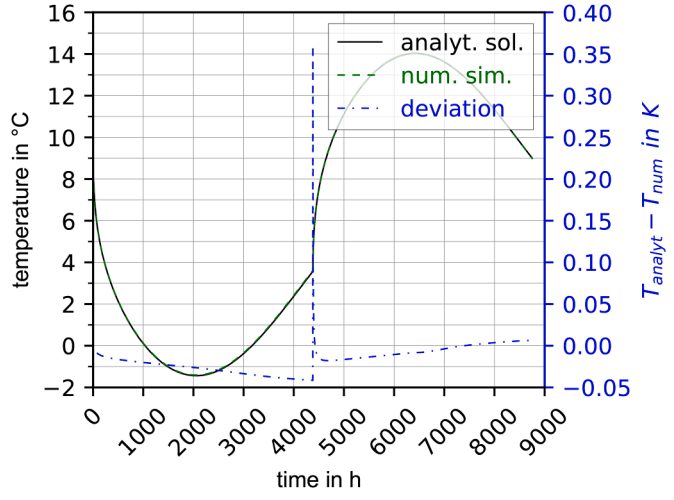

Fig. 10. Comparison of the mean temperature at the collector wall of the analytical and the numerical model for a constant heat extraction rate over 4380 h and a seasonal temperature variation at the ground surface.

Table 3
Experiment descriptions and results.

Description	Unit	Experiment 1	Experiment 2	Experiment 3
Date of the experiment	DD.MM.YYY	28.04.2022 – 03.05.2022	28.02.2023 – 6.03.2023	06.04.2023 – 11.04.2023
Heat injection rate	kW	0.88	1.51	1.54
Volume flow	m^3/h	1.00	0.88	0.88
Undisturbed temperature	°C	8.9	6.2	8.1
Thermal conductivity	W/(m·K)	1.47	1.84	1.76
Collector resistance	$(m^2 \cdot K)/W$	0.0245	0.0303	0.0233

season, i.e., from November to April in the northern hemisphere. In the cases where no active regeneration is foreseen, the ground heat collector uses natural regeneration during the summer half of the year (from May to October in the northern hemisphere) to be able to ensure the same amount of heat extraction the following year. For representing such conditions, the last verification scenario applies six months of constant heat extraction followed by six months of natural regeneration. Fig. 10 shows the results of both the analytical and the numerical model for the afore-described heat extraction profile. A very good match is achieved between both models. The deviation only increases abruptly as the heat extraction stops but decreases again afterwards. Apart from this short switchover time, the deviation is smaller than 0.05 K.

Based on the various model comparisons, it can be stated that the analytical model corresponds very well to the numerical model. After the successful verification, the next step is the validation of the analytical model with measurement data.

3.2. Validation of the analytical model

In order to demonstrate the practical applicability of the FPS model, a comparison with measurement data is performed. Three experiments were conducted, in each of which a constant volume flow and heat transfer rate were employed to the trench collector at the field site similar to a standard TRT for borehole heat exchangers (Spitler and Gehlin 2015). The main parameters of the experiments, the determined undisturbed subsurface temperatures, the estimated thermal conductivities, and collector resistances are listed in Table 3 for each experiment. The three experiments were carried out under slightly different conditions. The first experiment was carried out in 2022 with the lowest heat injection rate of 0.88 kW to avoid excessive overheating of the subsurface, since the undisturbed subsurface temperature was rather high at that time. The two other experiments were conducted in spring 2023 starting with considerably lower undisturbed subsurface temperatures, especially for experiment 2. This range of possible different initial parameters creates a solid basis for validating the analytical model. The constant heat injection rate and the constant volume flow are induced by the TRT device. For all experiments, first the undisturbed subsurface temperature at the installation depth was determined using the buried PT100 sensors directly next to the collector. Then, a fitting procedure, i.e. the Levenberg-Marquardt algorithm for nonlinear least squares curve-fitting problems, was conducted to estimate the thermal conductivity, λ, and the collector resistance, R_c. To avoid the influence of the starting behaviour, the measurement data within the first hour was neglected.

A comparison of the measurement data and the FPS model is shown in Figs. 11–13. These figures show a good agreement for all three experiments. However, it is noticeable that the fitted values for the thermal

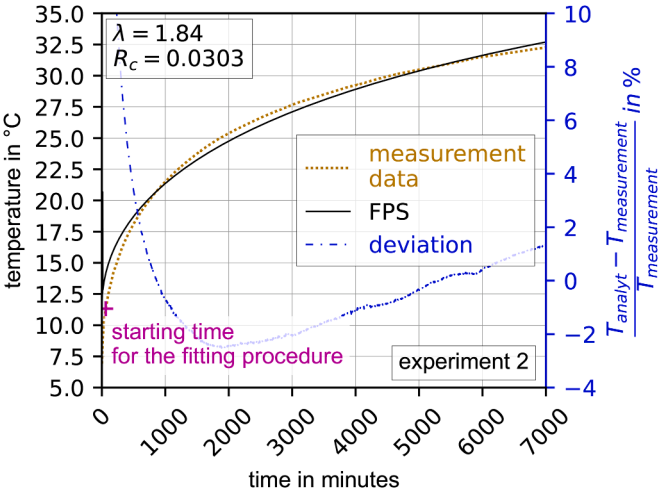

Fig. 12. Comparison of the finite plane source and the measurement data of experiment 2.

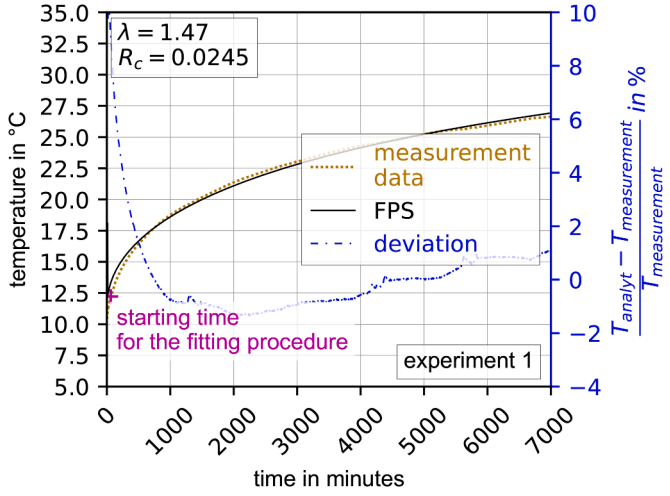

Fig. 11. Comparison of the finite plane source and the measurement data of experiment 1.

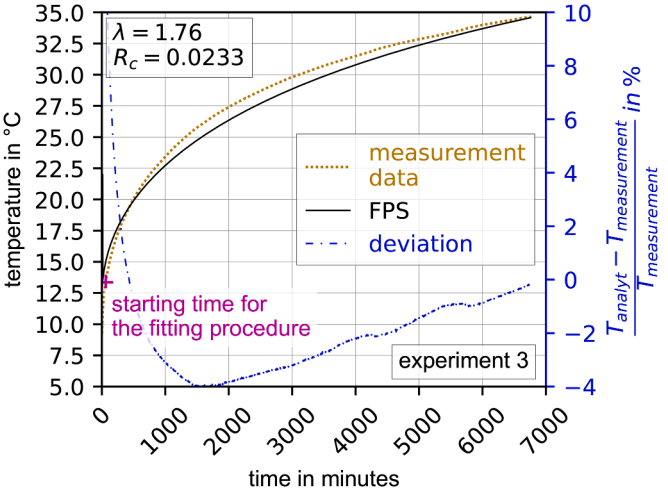

Fig. 13. Comparison of the finite plane source and the measurement data of experiment 3.

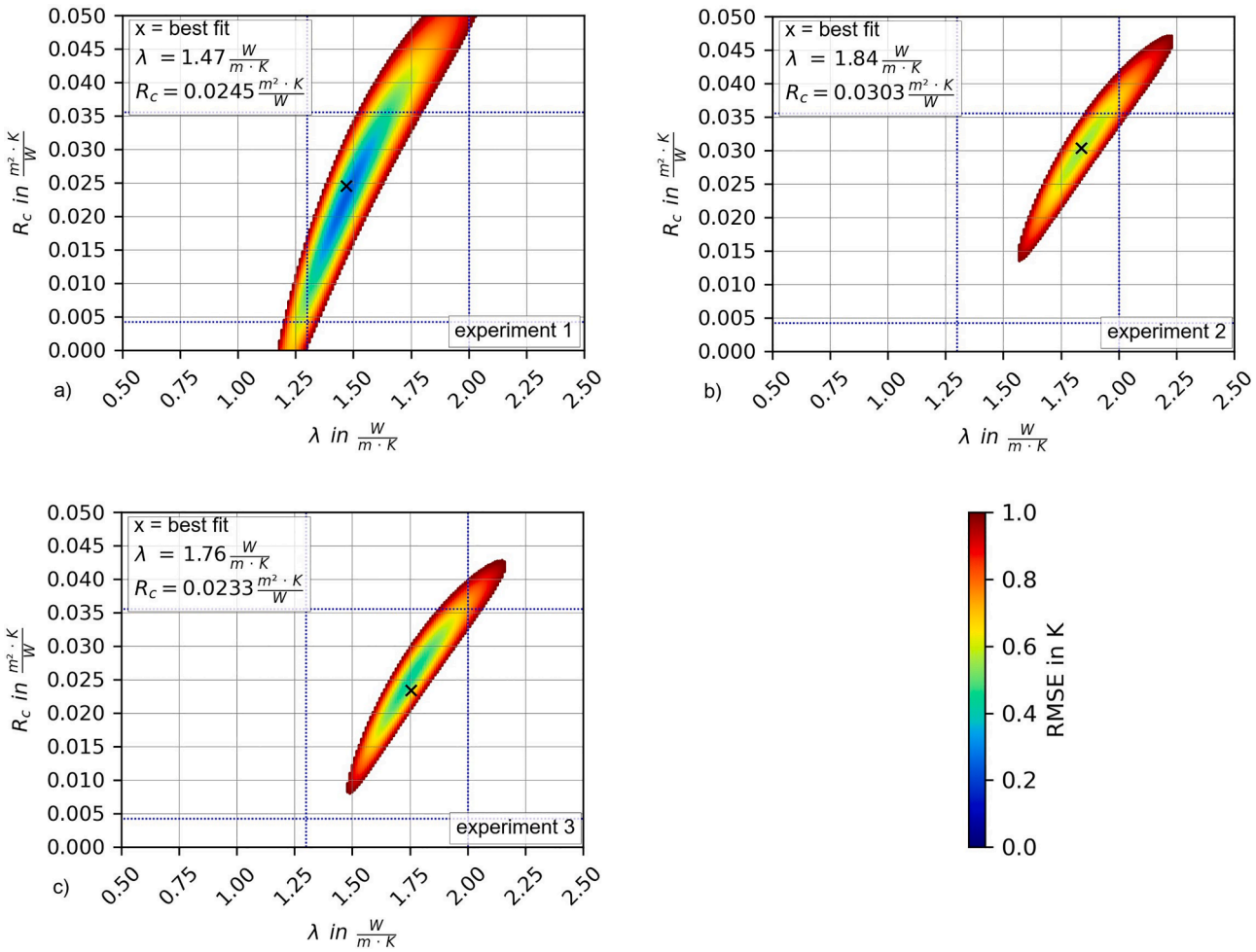

Fig. 14. RMSE of the collector resistance and the thermal conductivity pairs for simulation of a) experiment 1, b) experiment 2, c) experiment 3.

conductivity and the collector resistance vary depending on the experiment. In particular, the range of thermal conductivity values is relatively wide, especially between the first experiment and the last two experiments. One reason for the higher thermal conductivities in the experiments of 2023 may be the fact that there was a relatively high precipitation in 2023 (Deutscher Wetterdienst, 2023). Related studies indicate that the influence of moisture may be significant for the heat conduction of a ground heat exchanger, especially in low-moisture soils (Li et al. 2022).

To evaluate the quality of the fitting and the resulting parameters for the thermal conductivity and the collector resistance, an exhaustive grid search was carried out for all experiments. The thermal conductivity was evaluated from 0.01 to 5.0 in 0.01 steps and the collector resistance from 0.0001 to 0.1 in 0.0001 steps leading to a total number of about 500,000 value pairs. The root mean square error (RMSE) for each pair of values is determined for all 3 experiments and visualised in Fig. 14 for RMSE-values less than or equal to 1 K. Physical thermal conductivity measurements of the soil at the site were conducted both in-situ and from bucket samples. The in-situ measurements are done with the hot wire method with a needle probe (ISOMET 2104, Applied Precision Ltd., Slovakia), whereas the bucket samples are conducted with the transient plane source method (HotDisk TPS1500, C3 Prozess- und Analysentechnik, Germany). The measurements showed values between 1.3 and 2.0 W/(m·K). As depicted in Fig. 14, the smallest deviation to the measurement data lies within this range. The steepness of the RMSE trend in the figures show that the thermal conductivity is very sensitive and, thus, can be estimated well. The feasible range of the collector resistance, however, is large. In complementary numerical simulations, the collector resistance for the installed collector type is determined to be 0.00429 (m^2·K)/W. However, as soon as the contact between the subsurface and the collector is not ideal, the resistance increases substantially. Even with an air gap of only 0.5 mm on both collector sides, the resistance triples. The real value of the collector resistance is likely to be higher than the simulated value due to the assumed ideal contact with the subsurface and the assumption of a uniform flow through the collector in the simulation model. As an upper limit, an air gap of 1.5 mm on both collector sides is added to the simulated resistance value, leading to a collector resistance of 0.03554 (m^2·K)/W. Furthermore, it is to be mentioned that the assumed uniform flow in the resistance model does not perfectly apply over the entire collector height in practice. For this reason, a higher collector resistance is to be expected. In addition, it is possible that, analogous to the finding of Marcotte and Pasquier (2008) for borehole resistances, the collector resistance is overestimated by the curve fitting based on the least-squares. As with the thermal conductivity, the collector resistance is also within the expected range due to the non-ideal connection to the subsurface and flow into the collector.

4. Conclusions

This paper presents a three-dimensional, analytical model for planar ground heat collectors vertically installed in trenches for dimensioning purposes. The model not only considers the correct geometry of the source system but also the seasonal temperature fluctuation in the ground as well as the thermal resistance through the heat exchanger plate and its influence on the fluid temperature in the collector. If the

subsurface parameters and the heat extraction or injection rate are known, the mean fluid temperature in the collector can be calculated for the case of pure heat conduction in the ground.

The FPS is used to represent the heat extraction or injection and the heat conduction in the subsurface. A mathematical solution for the quadruple integrals of the FPS is presented containing only double or single integrals. A dimensional analysis is performed which allows the use of dimensionless temperature responses to cover a wider range of similar geometries. Furthermore, a mathematical solution for the spatially averaged seasonal temperature variation over the installation depth of the collector is presented and the use of a ground heat exchanger resistance is introduced. The calculation algorithm presented uses the superposition principle of all the aforementioned temperature responses in order to determine the mean fluid temperature in the ground heat collector.

The developed novel model was verified with numerical simulations and validated satisfactorily with measured values of an experimental plant. Compared to numerical simulations, which do not even directly calculate the mean fluid temperature, the calculation time of the presented analytical model is 60 times smaller. Characterised by a lower complexity, analytical models in general are easier to handle and therefore more suitable for dimensioning and extensive parameter studies.

These promising results should be further investigated to be able to map load profiles of ground heat collectors through temporal superposition in the analytical model. Finally, it is strongly recommended to extend the analytical model to take the phase change within the subsurface into account since ground heat collectors are characterised by freezing the ground during winter.

Funding

This work was financially supported by the Federal Ministry for Economic Affairs and Climate Action of Germany (grant number 03EE4020A) and by the EU Horizon Europe project INTERSTORES (project no. 101136100).

CRediT authorship contribution statement

Adinda Van de Ven: Methodology, Software, Validation, Formal analysis, Investigation, Data curation, Writing – original draft, Visualization, Project administration, Funding acquisition. **Peter Bayer:** Conceptualization, Writing – review & editing, Supervision. **Roland Koenigsdorff:** Conceptualization, Methodology, Writing – review & editing, Supervision, Project administration, Funding acquisition.

Declaration of competing interest

The authors declare the following financial interests/personal relationships which may be considered as potential competing interests:

Adinda Van de Ven reports financial support was provided by Federal Ministry for Economic Affairs and Climate Action. Peter Bayer reports financial support was provided by European Commission. If there are other authors, they declare that they have no known competing financial interests or personal relationships that could have appeared to influence the work reported in this paper.

Data availability

Data will be made available on request.

Acknowledgements

We would like to thank Stefan Hofmann for his support in calculus and Andreas Köhler for his support with the experiments. We thank Ryan Pearson for proof reading and Anna Albers for her work on the physical measurements of the subsurface properties. Finally, we gratefully acknowledge the valuable comments of the two anonymous reviewers.

Appendix

Computationally optimised solution of the mean result of the FPS:

$$\overline{T}_{FPS}(y,t) = \frac{\dot{q}}{4\ \pi\ \lambda\ L_c\ H_c} \tag{A I}$$

$$(a+b+c+d+e+f+g+h+i+j+k+l+m+n+o+p+q+r)$$

$$a = \frac{4}{3}\left((y^2)^{\frac{3}{2}} erfc\left(\sqrt{\frac{y^2}{4\alpha t}}\right) - \sqrt{\frac{4\alpha t}{\pi}}\,(4\alpha t + y^2) e^{\frac{-y^2}{4\alpha t}} \right)$$

$$-\left(y^2 + {H_c}^2\right)^{\frac{3}{2}} erfc\left(\sqrt{\frac{y^2+{H_c}^2}{4\alpha t}}\right) + \sqrt{\frac{4\alpha t}{\pi}}\left(4\alpha t + y^2 + {H_c}^2\right) e^{\frac{-y^2-{H_c}^2}{4\alpha t}}$$

$$-\left({L_c}^2 + y^2\right)^{\frac{3}{2}} erfc\left(\sqrt{\frac{{L_c}^2+y^2}{4\alpha t}}\right) + \sqrt{\frac{4\alpha t}{\pi}}\left(4\alpha t + {L_c}^2 + y^2\right) e^{\frac{-{L_c}^2-y^2}{4\alpha t}} \tag{A II}$$

$$+\left({L_c}^2 + y^2 + {H_c}^2\right)^{\frac{3}{2}} erfc\left(\sqrt{\frac{{L_c}^2+y^2+{H_c}^2}{4\alpha t}}\right)$$

$$+\sqrt{\frac{4\alpha t}{\pi}}\left(4\alpha t + {L_c}^2 + y^2 + {H_c}^2\right) e^{\frac{-{L_c}^2-y^2-{H_c}^2}{4\alpha t}}$$

$$b = \frac{2}{\sqrt{\pi}}(4\alpha t)^{\frac{3}{2}}\left(e^{\frac{-y^2}{4\alpha t}} - e^{\frac{-y^2-{H_c}^2}{4\alpha t}} - e^{\frac{-{L_c}^2-y^2}{4\alpha t}} + e^{\frac{-{L_c}^2-y^2-{H_c}^2}{4\alpha t}} \right) \tag{A III}$$

$$c = -8\ \alpha\ t\ L_c\left(e^{\frac{-y^2}{4\alpha t}} - e^{\frac{-y^2-{H_c}^2}{4\alpha t}} \right) erf\left(\frac{L_c}{\sqrt{4\alpha t}}\right) \tag{A IV}$$

$$d = -8\ \alpha\ t\ H_c\left(e^{\frac{-y^2}{4\alpha t}} - e^{\frac{-{L_c}^2-y^2}{4\alpha t}}\right) erf\left(\frac{H_c}{\sqrt{4\alpha t}}\right) \tag{A V}$$

$$e = 2L_c\sqrt{4\alpha t}$$
$$\int_{-L_c}^{L_c} \sqrt{\frac{\mu^2+y^2}{4\alpha t}} erfc\left(\sqrt{\frac{\mu^2+y^2}{4\alpha t}}\right) - \sqrt{\frac{\mu^2+y^2+H_c^2}{4\alpha t}} erfc\left(\sqrt{\frac{\mu^2+y^2+H_c^2}{4\alpha t}}\right) d\mu \tag{A VI}$$

$$f = 2\ H_c\ \sqrt{4\alpha t}$$
$$\int_{-H_c}^{H_c} \sqrt{\frac{y^2+\zeta^2}{4\alpha t}}\ erfc\left(\sqrt{\frac{y^2+\zeta^2}{4\alpha t}}\right) - \sqrt{\frac{L_c^2+y^2+\zeta^2}{4\alpha t}}\ erfc\left(\sqrt{\frac{L_c^2+y^2+\zeta^2}{4\alpha t}}\right) d\zeta \tag{A VII}$$

$$g = L_c\ H_c\ \sqrt{4\alpha t} \int_{-H_c}^{H_c}\int_{-L_c}^{L_c} \frac{erfc\left(\sqrt{\frac{\mu^2+y^2+\zeta^2}{4\alpha t}}\right)}{\sqrt{\mu^2+y^2+\zeta^2}}\ d\mu\ d\zeta \tag{A VIII}$$

$$h = \frac{2}{3}\left(\begin{array}{l} 2\left[\begin{array}{l}\left(y^2+(H_{inst}+H_{tot})^2\right)^{\frac{3}{2}} erfc\left(\sqrt{\frac{y^2+(H_{inst}+H_{tot})^2}{4\alpha t}}\right) \\ -\sqrt{\frac{4\alpha t}{\pi}}\left(4\alpha t+y^2+(H_{inst}+H_{tot})^2\right)e^{\frac{-y^2-(H_{inst}+H_{tot})^2}{4\alpha t}}\end{array}\right] \\ -\left(y^2+(2H_{inst})^2\right)^{\frac{3}{2}} erfc\left(\sqrt{\frac{y^2+(2H_{inst})^2}{4\alpha t}}\right) \\ +\sqrt{\frac{4\alpha t}{\pi}}\left(4\alpha t+y^2+(2H_{inst})^2\right)e^{\frac{-y^2-(2H_{inst})^2}{4\alpha t}} \\ -\left(y^2+(2H_{tot})^2\right)^{\frac{3}{2}} erfc\left(\sqrt{\frac{y^2+(2H_{tot})^2}{4\alpha t}}\right) \\ +\sqrt{\frac{4\alpha t}{\pi}}\left(4\alpha t+y^2+(2H_{tot})^2\right)e^{\frac{-y^2-(2H_{tot})^2}{4\alpha t}}\end{array}\right) \tag{A IX}$$

$$i = -\frac{2}{3}$$
$$\left(\begin{array}{l} 2\left[\begin{array}{l}\left(L_c^2+y^2+(H_{inst}+H_{tot})^2\right)^{\frac{3}{2}} erfc\left(\sqrt{\frac{L_c^2+y^2+(H_{inst}+H_{tot})^2}{4\alpha t}}\right) \\ -\sqrt{\frac{4\alpha t}{\pi}}\left(4\alpha t+L_c^2+y^2+(H_{inst}+H_{tot})^2\right)e^{\frac{-L_c^2-y^2-(H_{inst}+H_{tot})^2}{4\alpha t}}\end{array}\right] \\ -\left(L_c^2+y^2+(2H_{inst})^2\right)^{\frac{3}{2}} erfc\left(\sqrt{\frac{L_c^2+y^2+(2H_{inst})^2}{4\alpha t}}\right) \\ +\sqrt{\frac{4\alpha t}{\pi}}\left(4\alpha t+L_c^2+y^2+(2H_{inst})^2\right)e^{\frac{-L_c^2-y^2-(2H_{inst})^2}{4\alpha t}} \\ -\left(L_c^2+y^2+(2H_{tot})^2\right)^{\frac{3}{2}} erfc\left(\sqrt{\frac{L_c^2+y^2+(2H_{tot})^2}{4\alpha t}}\right) \\ +\sqrt{\frac{4\alpha t}{\pi}}\left(4\alpha t+L_c^2+y^2+(2H_{tot})^2\right)e^{\frac{-L_c^2-y^2-(2H_{tot})^2}{4\alpha t}}\end{array}\right) \tag{A X}$$

$$j = \frac{(4\alpha t)^{\frac{3}{2}}}{\sqrt{\pi}}\left(2e^{\frac{-y^2-(H_{inst}+H_{tot})^2}{4\alpha t}} - e^{\frac{-y^2-(2H_{inst})^2}{4\alpha t}} - e^{\frac{-y^2-(2H_{tot})^2}{4\alpha t}}\right) \tag{A XI}$$

$$k = -\frac{(4\alpha t)^{\frac{3}{2}}}{\sqrt{\pi}} \left(2e^{\frac{-L_c^2-y^2-(H_{inst}+H_{tot})^2}{4\alpha t}} - e^{\frac{-L_c^2-y^2-(2H_{inst})^2}{4\alpha t}} - e^{\frac{-L_c^2-y^2-(2H_{tot})^2}{4\alpha t}}\right) \tag{A XII}$$

$$l = -4\alpha t L_c \left(2e^{\frac{-y^2-(H_{inst}+H_{tot})^2}{4\alpha t}} - e^{\frac{-y^2-(2H_{inst})^2}{4\alpha t}} - e^{\frac{-y^2-(2H_{tot})^2}{4\alpha t}}\right) erf\left(\frac{L_c}{\sqrt{4\alpha t}}\right) \tag{A XIII}$$

$$m = 2\alpha t\left(e^{\frac{-y^2}{4\alpha t}} - e^{\frac{-L_c-y^2}{4\alpha t}}\right) \begin{pmatrix} 4(H_{inst}+H_{tot})erf\left(\frac{(H_{inst}+H_{tot})}{\sqrt{4\alpha t}}\right) \\ -4H_{inst}\ erf\left(\frac{2H_{inst}}{\sqrt{4\alpha t}}\right) - 4H_{tot}\ erf\left(\frac{2H_{tot}}{\sqrt{4\alpha t}}\right) \end{pmatrix} \tag{A XIV}$$

$$n = L_c\sqrt{4\alpha t} \int_{-L_c}^{L_c} 2\sqrt{\frac{\mu^2+y^2+(H_{inst}+H_{tot})^2}{4\alpha t}}\ erfc\left(\sqrt{\frac{\mu^2+y^2+(H_{inst}+H_{tot})^2}{4\alpha t}}\right) - \sqrt{\frac{\mu^2+y^2+(2H_{inst})^2}{4\alpha t}}\ erfc\left(\sqrt{\frac{\mu^2+y^2+(2H_{inst})^2}{4\alpha t}}\right) - \sqrt{\frac{\mu^2+y^2+(2H_{tot})^2}{4\alpha t}}\ erfc\left(\sqrt{\frac{\mu^2+y^2+(2H_{tot})^2}{4\alpha t}}\right) d\mu \tag{A XV}$$

$$o = 4H_{inst}\sqrt{4\alpha t} \int_{2H_{inst}}^{H_{inst}+H_{tot}} \sqrt{\frac{L_c^2+y^2+\eta^2}{4\alpha t}}\ erfc\left(\sqrt{\frac{L_c^2+y^2+\eta^2}{4\alpha t}}\right) - \sqrt{\frac{y^2+\eta^2}{4\alpha t}}\ erfc\left(\sqrt{\frac{y^2+\eta^2}{4\alpha t}}\right) d\eta \tag{A XVI}$$

$$p = 4H_{tot}\sqrt{4\alpha t} \int_{H_{inst}+H_{tot}}^{2H_{tot}} \sqrt{\frac{y^2+\eta^2}{4\alpha t}}\ erfc\left(\sqrt{\frac{y^2+\eta^2}{4\alpha t}}\right) - \sqrt{\frac{L_c^2+y^2+\eta^2}{4\alpha t}}\ erfc\left(\sqrt{\frac{L_c^2+y^2+\eta^2}{4\alpha t}}\right) d\eta \tag{A XVII}$$

$$q = -2H_{inst}L_c \int_{2H_{inst}}^{H_{inst}+H_{tot}} \int_{-L_c}^{L_c} \frac{erfc\left(\sqrt{\frac{\mu^2+y^2+\eta^2}{4\alpha t}}\right)}{\sqrt{\mu^2+y^2+\eta^2}}\ d\mu\ d\eta \tag{A XVIII}$$

$$r = 2H_{tot}L_c \int_{H_{inst}+H_{tot}}^{2H_{tot}} \int_{-L_c}^{L_c} \frac{erfc\left(\sqrt{\frac{\mu^2+y^2+\eta^2}{4\alpha t}}\right)}{\sqrt{\mu^2+y^2+\eta^2}}\ d\mu\ d\eta \tag{A XIX}$$

References

Amadeh, A., Habibi, M., Hakkaki-Fard, A., 2020. Numerical simulation of a ground-coupled heat pump system with vertical plate heat exchangers: a comprehensive parametric study. Geothermics. https://doi.org/10.1016/j.geothermics.2020.101913.

Bortoloni, M., Bottarelli, M., 2015. On the sizing of a flat-panel ground heat exchanger. Int. J. Energy Environ. Eng. https://doi.org/10.1007/s40095-014-0150-0.

Bottarelli, M., Di Federico, V., 2012. Numerical comparison between two advanced HGHEs. Int. J. Low-Carbon Technolog. https://doi.org/10.1093/ijlct/ctr050.

Bottarelli, M., Fujii, H., Di Federico, V., 2014. Performance of a drainage trench employed as ground heat exchanger. In: International Heat Transfer Conference, p. 15.

Bottarelli, M., Bortoloni, M., Su, Y., 2019. On the sizing of a novel Flat-Panel ground heat exchanger in coupling with a dual-source heat pump. Renew. Energy. https://doi.org/10.1016/j.renene.2019.04.088.

Bottarelli, M., 2013. A preliminary testing of a flat panel ground heat exchanger. Int. J. Low-Carbon Technolog. https://doi.org/10.1093/ijlct/ctt003.

Cao, J., Bottarelli, M., Bortoloni, M., Pei, G., 2018. Small-scale lab analysis of the ground freezing effect on the thermal performance of a Flat-Panel ground heat exchanger. Geothermics. https://doi.org/10.1016/j.geothermics.2018.03.013.

Carslaw, H.S., Jaeger, J.C., 1980. Conduction of Heat in Solids. Clarendon, Oxford.

Cimmino, M., 2018. Fast calculation of the g -functions of geothermal borehole fields using similarities in the evaluation of the finite line source solution. J. Build. Perform. Simul. https://doi.org/10.1080/19401493.2017.1423390.

Ciriello, V., Bottarelli, M., Di Federico, V., 2015a. Uncertainty-based Analysis of Variations in Subsurface Thermal Field Due to Horizontal Flat-panel Heat Exchangers.

Ciriello, V., Bottarelli, M., Di Federico, V., Tartakovsky, D.M., 2015b. Temperature fields induced by geothermal devices. Energy. https://doi.org/10.1016/j.energy.2015.10.052.

Deutscher Wetterdienst, 2023. Deutschlandwetter im Jahr 2023: Erwärmungstrend hält an: 2023 mit neuem Rekord und reichlich Niederschlag. Offenbach, Germany. Available at https://www.dwd.de/DE/presse/pressemitteilungen/DE/2023/20231229_deutschlandwetter_jahr2023_news.html. Accessed 28 Mar 2024.

Eskilson, P., 1987. Thermal analysis of heat extraction boreholes. PhD. Thesis. University of Lund, Sweden, Department of Mathematical Physics.

Fascì, M.L., Lazzarotto, A., Acuña, J., Claesson, J., 2021. Simulation of thermal influence between independent geothermal boreholes in densely populated areas. Appl. Therm. Eng. https://doi.org/10.1016/j.applthermaleng.2021.117241.

Gabrielli, L., Bottarelli, M., 2016. Financial and economic analysis for ground-coupled heat pumps using shallow ground heat exchangers. Sustain. Citi. Soc. https://doi.org/10.1016/j.scs.2015.09.008.

Gerola, M., Cecinato, F., Haasnoot, J.K., Vardon, P.J., 2023. Understanding the thermal efficiency of energy Quay Walls: a comprehensive study using field tests and finite element simulations. In: Comsol conference Munich, 2023, pp. 1–6.

Habibi, M., Amadeh, A., Hakkaki-Fard, A., 2020. A numerical study on utilizing horizontal flat-panel ground heat exchangers in ground-coupled heat pumps. Renew. Energy. https://doi.org/10.1016/j.renene.2019.09.040.

Hellström, G., 1991. Ground Heat storage: Thermal Analyses of Duct Storage systems. Disseration. Lund University, Department of Mathematical Physics.

Hou, G., Taherian, H., Song, Y., Jiang, W., Chen, D., 2022. A systematic review on optimal analysis of horizontal heat exchangers in ground source heat pump systems. Renew. Sustain. Energy Rev. https://doi.org/10.1016/j.rser.2021.111830.

Kürten, S., Mottaghy, D., Ziegler, M., 2015. A new model for the description of the heat transfer for plane thermo-active geotechnical systems based on thermal resistances. Acta Geotechnica. https://doi.org/10.1007/s11440-014-0311-6.

Koenigsdorff, R., 2011. Oberflächennahe Geothermie für Gebäude: Grundlagen und Anwendungen Zukunftsfähiger Heizung und Kühlung. Fraunhofer IRB-Verl, Stuttgart.

Kusuda, T., Achenbach, P.R., 1965. Earth Temperature and Thermal Diffusivity at Selected Stations in the United States.

Lamarche, L., 2021. Analytic models and effective resistances for coaxial ground heat exchangers. Geothermics. https://doi.org/10.1016/j.geothermics.2021.102224.

Larwa, B., Teper, M., Grzywacz, R., Kupiec, K., 2019. Study of a slinky-coil ground heat exchanger – comparison of experimental and analytical solution. Int. J. Heat Mass Transf. https://doi.org/10.1016/j.ijheatmasstransfer.2019.118438.

Li, S., Sun, T., Du, Y., Li, M., 2022. Influence of moisture on heat transfer of ground heat exchangers in unsaturated soils. Renew. Energy. https://doi.org/10.1016/j.renene.2022.04.073.

Marcotte, D., Pasquier, P., 2008. On the estimation of thermal resistance in borehole thermal conductivity test. Renew. Energy. https://doi.org/10.1016/j.renene.2008.01.021.

MEFA Befestigungs- und Montagesysteme GmbH, 2022. Regenerative Energiequellen für Wärmepumpen: Planungs- und Bedienungsanleitung. Available at. https://www.mefa.de/Energy%20Systems/Dokumente/MEFA%20geo%20Planungs-Betriebsanleitung.pdf. Accessed 21 Jun 2024.

Miocic, J.M., Schleichert, L., Van de Ven, A., Koenigsdorff, R., 2024. Fast calculation of the technical shallow geothermal energy potential of large areas with a steady-state solution of the finite line source. Geothermics. https://doi.org/10.1016/j.geothermics.2023.102851.

Oh, H., Beckers, K., 2023. Cost and Performance Analysis for Five Existing Geothermal Heat Pump-Based District Energy Systems in the United States.

Ozudogru, T.Y., Olgun, C.G., Senol, A., 2014. 3D numerical modeling of vertical geothermal heat exchangers. Geothermics. https://doi.org/10.1016/j.geothermics.2014.02.005.

Ramming, K., 2007. Bewertung und Optimierung oberflächennaher Erdwärmekollektoren für Verschiedene Lastfälle. TUDpress, Dresden. Rashid, F.L., Dhaidan, N.S., Hussein, A.K., Al-Mousawi, F.N., Younis, O., 2023. Ground heat exchanger in different configuration: review of recent advances and development. Geoenergy Sci. Eng. https://doi.org/10.1016/j.geoen.2023.211872.

Rivera, J.A., Blum, P., Bayer, P., 2015. Analytical simulation of groundwater flow and land surface effects on thermal plumes of borehole heat exchangers. Appl. Energy. https://doi.org/10.1016/j.apenergy.2015.02.035.

Rivera, J.A., Blum, P., Bayer, P., 2017. Increased ground temperatures in urban areas: estimation of the technical geothermal potential. Renew. Energy. https://doi.org/10.1016/j.renene.2016.11.005.

Schramek, E.-R., Recknagel, H., Sprenger, E., 2005. Taschenbuch für Heizung und Klimatechnik: Einschließlich Warmwasser- und Kältetechnik : mit über 2100 Abbildungen und über 350 Tafeln sowie 4 Einschlagtafeln. Oldenbourg Industrieverlag, München.

Schwarz, H., Jocic, N., Bertermann, D., 2022. Development of a calculation concept for mapping specific heat extraction for very shallow geothermal systems. Sustainability. https://doi.org/10.3390/su14074199.

Spitler, J.D., Gehlin, S.E., 2015. Thermal response testing for ground source heat pump systems—an historical review. Renew. Sustain. Energy Rev. https://doi.org/10.1016/j.rser.2015.05.061.

Suft, O., Bertermann, D., 2022. Long-term monitoring of a very shallow horizontal collector system. In: European Geothermal Congress, 2022, pp. 1–6. Proceedings.

Van de Ven, A., Koenigsdorff, R., Hofmann, S., 2018. Entwicklung konsistenter Auslegungsmodelle für oberflächennahe geothermische Quellensysteme. BauSIM 2018: 7. Deutsch-Österreichische IBPSA-Konferenz, pp. 508–515.

Van de Ven A., Koenigsdorff R., Neth F., Köhler A., Steger H., Albers A., Schindler L. (unpublished results). Behaviour of the Subsurface as a Reaction on an Operating Planar Trench Collector. Manuscript in preparation.

Verein Deutscher Ingenieure e.V., 2019. Thermische Nutzung des Untergrunds: Erdgekoppelte Wärmepumpenanlagen. Beuth Verlag GmbH, Berlin.

Wagner, V., Blum, P., Kübert, M., Bayer, P., 2013. Analytical approach to groundwater-influenced thermal response tests of grouted borehole heat exchangers. Geothermics. https://doi.org/10.1016/j.geothermics.2012.10.005.

Xiong, Z., Fisher, D.E., Spitler, J.D., 2015. Development and validation of a Slinky™ ground heat exchanger model. Appl. Energy. https://doi.org/10.1016/j.apenergy.2014.11.058.

Yoon, S., Lee, S.-R., Go, G.-H., 2014. A numerical and experimental approach to the estimation of borehole thermal resistance in ground heat exchangers. Energy. https://doi.org/10.1016/j.energy.2014.04.104.

Zhou, Y., Bidarmaghz, A., Makasis, N., Narsilio, G., 2021. Ground-source heat pump systems: the effects of variable trench separations and pipe configurations in horizontal ground heat exchangers. Energies. https://doi.org/10.3390/en14133919.